Available online at www.sciencedirect.com
ScienceDirect
Trans. Nonferrous Met. Soc. China 26(2016) 1379−1387
Transactions of Nonferrous Metals Society of China
www.tnmsc.cn

Microstructures and electrochemical corrosion properties of Mg−Al−Pb and Mg−Al−Pb−Ce anode materials

Yan FENG[1,2], Li LIU[1,2], Ri-chu WANG[1,2], Chao-qun PENG[1,2], Nai-guang WANG[1,2]

1. School of Materials Science and Engineering, Central South University, Changsha 410083, China;
2. Key Laboratory of Nonferrous Metal Materials Science and Engineering, Ministry of Education, Central South University, Changsha 410083, China

Received 29 June 2015; accepted 2 March 2016

Abstract: Mg−Al−Pb alloy is a good candidate for the anode material of magnesium seawater battery. For improving the low current utilization efficiency of Mg−Al−Pb alloy, the influence of Ce on the microstructures and electrochemical corrosion properties in a 3.5% NaCl solution was investigated using scanning electron microscope and electrochemical measurements. The results indicate that Ce refines the grain structure of Mg−Al−Pb alloy. The formation of strip $Al_{11}Ce_3$ second phase promotes the uniform distribution of $Mg_{17}Al_{12}$ phase in Mg−Al−Pb−Ce alloy. The addition of cerium accelerates the discharge activity of Mg−Al−Pb alloy. Due to a large number of cathodic $Al_{11}Ce_3$ and $Mg_{17}Al_{12}$ phases, Ce promotes the micro-galvanic corrosion and leads to larger corrosion current density and hydrogen evolution rate in Mg−Al−Pb−Ce alloy than those in Mg−Al−Pb alloy. However, Mg−Al−Pb alloy expresses smaller utilization efficiency than Mg−Al−Pb−Ce alloy because of grain detachment.
Key words: magnesium alloy; seawater battery; hydrogen evolution rate; discharge activity; utilization efficiency

1 Introduction

Seawater batteries provide higher practicability and lower cost than lithium or alkaline batteries for submarine applications [1,2]. Magnesium alloys are widely used as anode materials in seawater batteries because of many advantages, such as rapid activation, low specific mass, negative standard electrode potential and high current capacity [3,4]. Since the 1960s, magnesium seawater batteries have been developed for a lot of military and commercial applications, such as torpedo, electromotive and unmanned underwater vehicle power source [5−7].

As common alloying elements, rare earth elements can effectively influence the alloying, degassing, cleaning and purification processes in magnesium alloys. Mg−RE phases have high melting point leading to improved mechanical properties in high-temperature of magnesium alloys [8,9]. The low electrode potentials of Mg−RE compounds provide weak corrosion reaction with magnesium matrix as well as improved corrosion resistance [10−12]. LV et al [12] found that the electrochemical activity and peak power density of Mg−H_2O_2 semi-fuel cells were improved by addition of Ce and Y to magnesium anode materials. LIU et al [13] also reported that rare earth element Ce or La can react with impurities such as Fe and Cu, resulting in a cleaning of magnesium alloys. The microstructure of AM60 magnesium alloy had been optimized by Ce or La addition which facilitates the formation of new phase (γ) enriched with Al and RE [14]. The new phase (γ), which has more noble potential, results in a improved corrosion resistance of AM60 magnesium alloy [15]. Ce addition in AM50 magnesium alloy promotes the formation of $Al_{11}Ce_3$ phase and reduces the amount of β-phase ($Mg_{17}Al_{12}$) [16]. The embedding of remaining impurities in $Al_{11}Ce_3$ phase and the improved stability of passive films accelerate the corrosion resistance of AMRE alloy. The influence of lanthanum on the electrochemical behavior of AZ31 magnesium alloy was studied [17]. Better corrosion resistance and electrochemical activity were obtained in AZ31 magnesium alloy in a 1.0 mol/L $MgSO_4$ solution due to the 0.04 mmol/L $La(CH_3COO)_3$

Foundation item: Project (2015JC3004) supported by Science and Technology Plan Projects of Hunan Province, China; Project (51401243) supported by the National Natural Science Foundation of China
Corresponding author: Ri-chu WANG; Tel/Fax: +86-731-88836638; E-mail: wrc@csu.edu.cn
DOI: 10.1016/S1003-6326(16)64242-5

addition agent. Hence, alloying with rare earth elements is an effective way to boost the performance of magnesium anode materials in seawater battery.

Mg−Al−Pb alloy is a good candidate for the anode material of magnesium seawater battery due to the activation elements aluminium and lead, which synergistically enhances the discharge activity of pure magnesium [18,19]. However, the low current utilization efficiency restricts the application of Mg−Al−Pb anode materials in seawater battery. Considering the improved battery properties of magnesium anode with Ce addition [12], it would be interesting to obtain a thorough understanding of the electrochemical corrosion behavior of Mg−Al−Pb−Ce alloy. In fact, the influence of rare earth elements on the corrosion behavior and electrochemical activity of Mg−Al−Pb anode materials has received little attention. The aim of this work is to find a better magnesium anode for seawater battery and gain some insight into the influence of Ce on the corrosion behaviour and electrochemical activity of Mg−Al−Pb alloy.

2 Experimental

2.1 Preparation of materials

Mg−Al−Pb and Mg−Al−Pb−Ce alloys, with chemical compositions shown in Table 1, were prepared by melting the ingots of pure magnesium (99.99%), pure aluminum (99.99%), pure lead (99.99%), and Mg−29%Ce master alloy in a resistance furnace at 1023 K under an argon atmosphere. The molten metals protected by sulfur powder and argon were poured into a water-cooled steel mould with dimensions of d125 mm × 420 mm and cooled down to room temperature. The chemical composition of the specimens to be used was determined by inductively coupled plasma atomic emission spectrometry (ICP-AES), and the data indicated that the relative deviation for the content of each element was less than ±5% while the content of each impurity was lower than 0.1%. The cast alloys were selected as the research subjects for evaluating their electrochemical corrosion performance.

Table 1 Chemical compositions of Mg−Al−Pb and Mg−Al−Pb−Ce alloys (mass fraction, %)

Sample	Al	Pb	Ce	Mg
Mg−Al−Pb alloy	6.0	5.0	0	Bal.
Mg−Al−Pb−Ce alloy	6.0	5.0	0.6	Bal.

2.2 Microstructure characterization

Microstructures of the specimens were analyzed using a scanning electron microscope (SEM: FEI-Quanta200), equipped with an electron probe microscope analysis (EPMA: JXA−8230) after the samples had been ground with SiC abrasive paper and polished with diamond grinding paste. A solution of 1 mL nitric acid, 1 mL acetic acid, 1 g oxalic acid and 50−80 mL distilled water was used as the etchant to reveal the grain boundaries. The phase structures of Mg−Al−Pb and Mg−Al−Pb−Ce alloys were identified with an X-ray diffraction meter with Cu K_α radiation. The scan range of 2θ was from 10° to 80° with a scan speed of 4 (°)/min. The XRD pattern for each alloy was analyzed with Jade 6 software.

2.3 Electrochemical measurements

Electrochemical measurements of Mg−Al−Pb and Mg−Al−Pb−Ce alloys were carried out using a CHI660D electrochemistry workstation and a CHI680 current amplifier in a static 3.5% NaCl solution at 298 K constantly. The specimens were polished with emery paper and buffed to a mirror finish with diamond grinding paste. Each of them was sealed with epoxy resin except for an exposed surface of 10 mm × 10 mm submitted to the electrochemical tests in a three-electrode cell. A platinum sheet was used as auxiliary electrode and a saturated calomel electrode (SCE) with a standard electrode potential of 0.2412 V (vs SHE) was used as reference electrode, and testing samples were used as working electrode.

The polarization curves were measured from the cathodic side at a scanning rate of 0.05 mV/s. Hydrogen evolution rates were measured by immersing the samples in a 3.5% NaCl solution at 298 K, using a flow-meter (ADM 3000, Agilent Technologies) to collect hydrogen evolution products of the reaction. The potential−time curves in the course of galvanostatic discharge for 600 s were obtained by imposing anodic current density of 180 mA/cm^2 on the testing samples. A solution of 200 g/L CrO_3 and 10 g/L $AgNO_3$ was used to remove the corrosion products after the samples had been tested, and then the corroded surfaces of the samples were observed with the Quanta−200 SEM using secondary electron image.

The utilization efficiency of each sample during the discharge process was given by the following relation [20,21]:

$$\eta = \frac{m_t}{m_a} \times 100\% \quad (1)$$

where η is the utilization efficiency (%), m_t is the theoretical mass loss (g) corresponding to the impressed current, and m_a is the actual mass loss (g) within the discharge period. The theoretical mass loss was calculated using Eq. (2) [14]:

$$m_t = \frac{It}{F\sum\left(\frac{X_i n_i}{M_i}\right)} \quad (2)$$

where I is the impressed current (A); t is the discharge time (s); F is the Faraday constant; X_i, n_i, and M_i are the mass fraction, ionic valence, and molar mass (g/mol) of an alloying element, respectively. In Eq. (2), the numerator is the discharge passing through the testing sample, and the denominator is the theoretical electric quantity delivered by one gram of testing sample. A solution of 200 g/L CrO_3 and 10 g/L $AgNO_3$ was also used to remove the discharge products after the testing samples had been discharged for a certain period. The actual mass loss was then obtained by subtracting the final mass of each sample from its initial mass. The discharge time at 180 mA/cm^2 was 1 h to achieve obvious mass loss to minimize the error [18].

3 Results and discussion

3.1 Microstructure analysis

Figure 1 shows the back scattering (BS) images of Mg−Al−Pb and Mg−Al−Pb−Ce alloys, whose X-ray diffraction patterns (XRD) are shown in Fig. 2. The electron probe microscope analysis of the second phases in Figs. 1(c) and (d) are described in Table 2. From Figs. 1(a, c), it can be seen that the second phases distribute discontinuously along the grain boundary in Mg−Al−Pb alloy. With the XRD results in Fig. 2(a) and EPMA results in Table 2, it can be deduced that the intergranular block second phase in Fig. 1(c) is $Mg_{17}Al_{12}$ compounds. Comparing with Mg−Al−Pb alloy, Mg−Al−Pb−Ce alloy expresses a refined microstructure with two second phases, as seen in Figs. 1(b) and (d). According to XRD results in Fig. 2(b) and EPMA results in Table 2, the second phases in Mg−Al−Pb−Ce alloy are dispersive strip $Al_{11}Ce_3$ compounds and block $Mg_{17}Al_{12}$ compounds, respectively. Moreover, the sizes of disperse $Mg_{17}Al_{12}$ phases decrease, leading to homogeneous distribution of $Mg_{17}Al_{12}$ phases in Mg−Al−Pb−Ce alloy.

From EPMA data in Table 2, it can be also inferred that lead is solid-solution element in Mg−Al−Pb and Mg−Al−Pb−Ce alloys. The bright areas (point C) surrounding intergranular $Mg_{17}Al_{12}$ phase in Fig. 1(c) are aluminum and lead enriched areas. Ce does not solid-solute in Mg matrix but mainly exists in $Al_{11}Ce_3$ and $Mg_{17}Al_{12}$ compounds.

3.2 Polarization curves

Figure 3 shows the polarization curves of Mg−Al−Pb and Mg−Al−Pb−Ce alloys in a 3.5% NaCl solution. These curves were used to evaluate the corrosion current densities by extrapolating the cathodic branches back to the corrosion potentials [5]. The potential range used for Tafel extrapolating is about

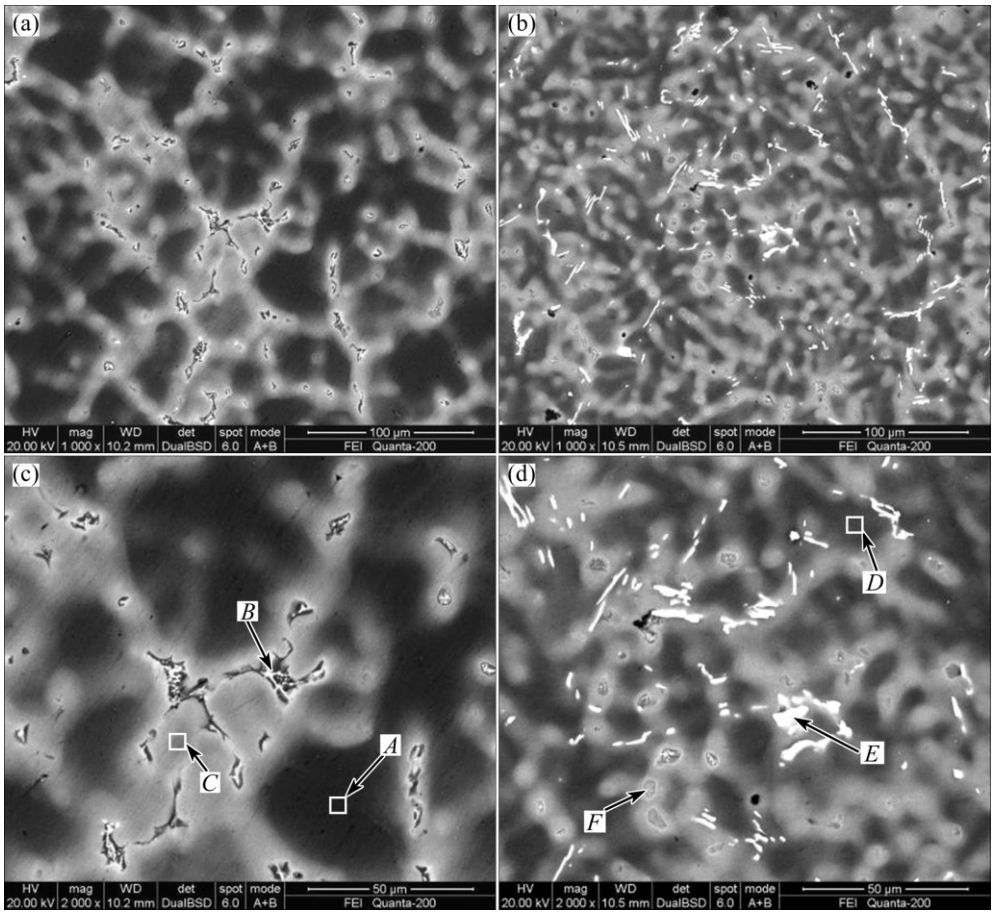

Fig. 1 Back scattering (BS) images of magnesium alloys: (a, c) Mg−Al−Pb alloy; (b, d) Mg−Al−Pb−Ce alloy

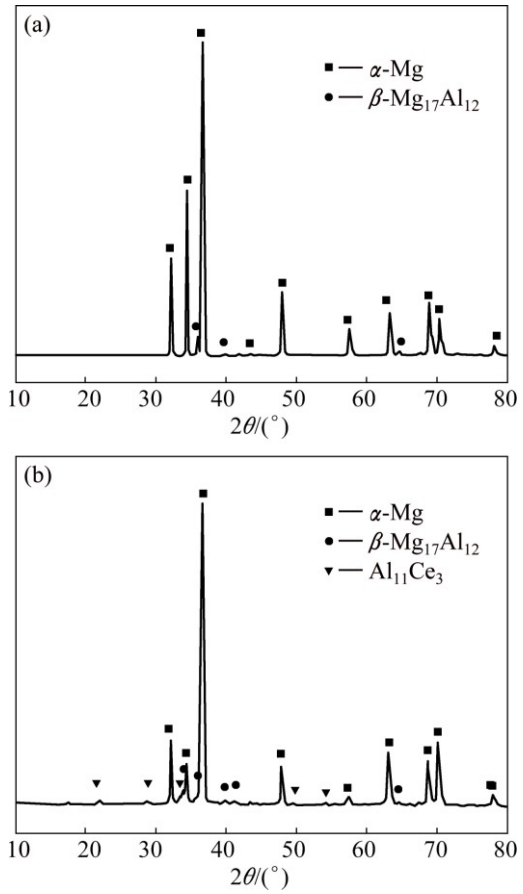

Fig. 2 XRD patterns of magnesium alloys: (a) Mg−Al−Pb alloy; (b) Mg−Al−Pb−Ce alloy

Table 2 Electron probe microscope analysis results of Mg−Al−Pb and Mg−Al−Pb−Ce alloys (mole fraction, %)

Sample	Point	Mole fraction/%				Phase analysis
		Mg	Al	Pb	Ce	
Mg−Al−Pb alloy	*A*	97.57	2.26	0.15	−	α-Mg
	B	68.92	30.45	0.59	0.05	β-$Mg_{17}Al_{12}$
	C	92.16	7.03	0.78	0.02	α-Mg
Mg−Al−Pb−Ce alloy	*D*	93.16	6.20	0.64	−	α-Mg
	E	44.77	43.67	0.26	11.22	γ-$Al_{11}Ce_3$
	F	70.50	28.79	0.65	0.07	β-$Mg_{17}Al_{12}$

120−250 mV more negative than the corrosion potential. The corrosion parameters derived from these polarization curves are listed in Table 3. For magnesium alloys, the evolution of hydrogen is the dominant feature and results in cathodic current at potentials more negative than the corrosion potential. While metal oxidation is the dominant feature and results in anodic current at potentials more positive than the corrosion potential. According to Fig. 3, it is obvious that the cathodic branches of Mg−Al−Pb and Mg−Al−Pb−Ce alloys show different trends. This certifies that Ce slightly changes the hydrogen evolution behaviour of Mg−Al−Pb alloy during cathodic polarization. According to Table 3, a larger corrosion current density (J_{corr}) of (45.1±1.2) μA/cm^2 is found in Mg−Al−Pb−Ce alloy. Therefore, Mg−Al−Pb−Ce alloy shows worse corrosion resistance than Mg−Al−Pb alloy. Meanwhile, the anodic Tafel slope (b_a) of Mg−Al−Pb−Ce alloy is found to be less than that of Mg−Al−Pb alloy. It can be deduced that the cerium addition in Mg−Al−Pb alloy promotes the anodic dissolution activity.

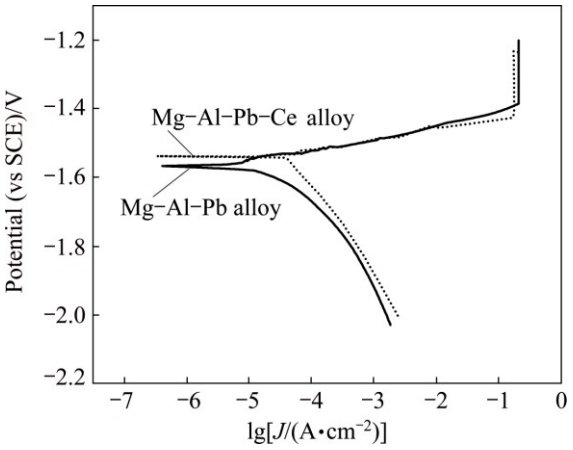

Fig. 3 Polarization curves of Mg−Al−Pb and Mg−Al−Pb−Ce alloys in 3.5% NaCl solution at 298 K

Table 3 Corrosion electrochemical parameters of Mg−Al−Pb and Mg−Al−Pb−Ce alloys from tests

Sample	J_{corr}/(μA·cm^{-2})	φ_{corr} (vs SCE)/V	B_a/(mV·dec^{-1})	v_{H_2}/(mL·cm^{-2}·h^{-1})
Mg−Al−Pb alloy	39.8±1.9	−1.567	38.25	1.02±0.01
Mg−Al−Pb−Ce alloy	45.1±1.2	−1.538	29.31	1.44±0.02

Sample	Average discharge potentials (vs SCE)/V	Utilization efficiency η/%
	180 mA/cm^2 for 600 s	180 mA/cm^2 for 1 h
Mg−Al−Pb alloy	−1.648	67.7±0.2
Mg−Al−Pb−Ce alloy	−1.756	74.7±0.4

3.3 Hydrogen evolution rate

Figure 4 shows the hydrogen evolution curves of Mg−Al−Pb and Mg−Al−Pb−Ce alloys in a 3.5% NaCl solution. The self-corrosion of magnesium alloys leads to hydrogen evolution. Larger hydrogen evolution rate leads to worse corrosion resistance in magnesium alloys. Actually, magnesium anode materials used in seawater battery usually serve at a large current density, which promotes hydrogen evolution and decreases anodic current efficiency. Hence, the hydrogen evolution

behaviours of Mg−Al−Pb and Mg−Al−Pb−Ce anode materials were discussed to improve their corrosion resistance during discharge. From Fig. 4, it can be seen that the hydrogen evolution processes of the alloys are smooth. The mean hydrogen evolution rate (v_{H_2}) is calculated and shown in Table 3. It can be seen that the mean hydrogen evolution rate increases from (1.02±0.01) to (1.44±0.02) mL/(cm^2·h^{-1}) with the addition of Ce to Mg−Al−Pb alloy. This is consistent with the corrosion current densities calculated from polarization curves tests.

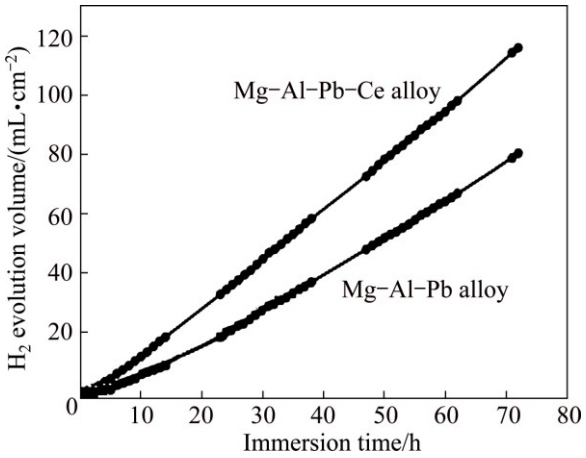

Fig. 4 Hydrogen generation curves of Mg−Al−Pb and Mg−Al−Pb−Ce alloys in 3.5% NaCl solution at 298 K

However, the results are contrary to previous researches, which reported that rare earth elements Ce or La can improve corrosion resistance of AM50, AM60 and AZ31 magnesium alloys [16,17]. In these alloys, the formation of γ-$Al_{11}Ce_3$ phase reduces the amount of cathodic β-phase ($Mg_{17}Al_{12}$) and improves stability of passive films, thus, accelerates the corrosion resistance of AMRE alloy. While in Mg−Al−Pb−Ce alloy as seen in Fig. 1, the formation of $Al_{11}Ce_3$ phase decreases the size of $Mg_{17}Al_{12}$ phase and inspires its disperse distribution. The dispersive small $Mg_{17}Al_{12}$ particles in magnesium matrix increase the effective surface area of the cathodic phases reversely. Thus, $Al_{11}Ce_3$ and $Mg_{17}Al_{12}$ phases accelerate the corrosion of magnesium matrix in Mg−Al−Pb−Ce alloy. The larger mean hydrogen evolution rate occurs in Mg−Al−Pb−Ce alloy. Figure 5 shows the surface morphologies of Mg−Al−Pb and Mg−Al−Pb−Ce alloys after hydrogen evolution tests with removing the corrosion products. According to Fig. 5(a), Mg−Al−Pb alloy suffers localized corrosion, with some shallow pits in localized regions. $Mg_{17}Al_{12}$ particles were found at the bottom of pits. The corrosion of magnesium matrix begins surrounding $Mg_{17}Al_{12}$ second phase because of its cathodic properties. According to Fig. 5(b), Mg−Al−Pb−Ce alloy suffers severely self-corrosion with a lot of deep pits on the corroded surface. The pit hole is so large that granular $Mg_{17}Al_{12}$ second phases were detached from the surface. But strip $Al_{11}Ce_3$ second phases are crisscross in magnesium matrix and remain during hydrogen evolution corrosion.

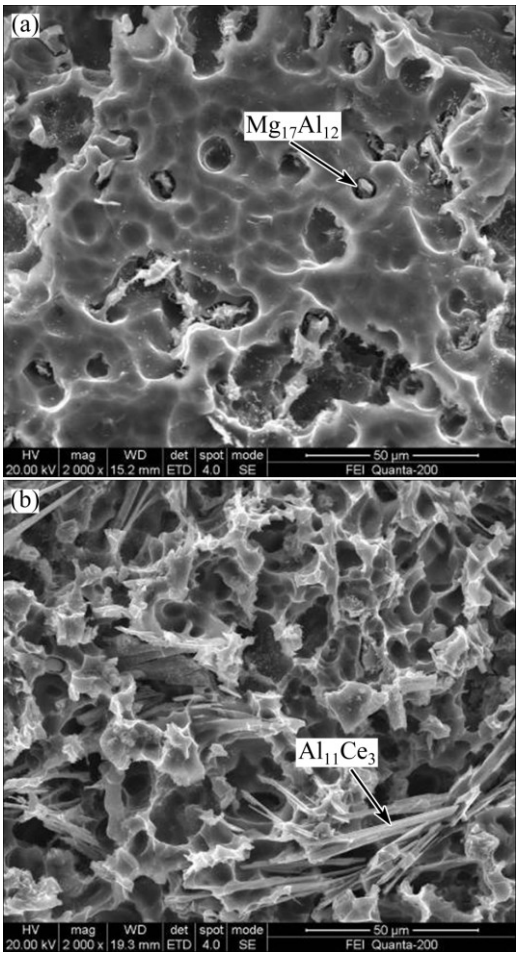

Fig. 5 Secondary electron (SE) images of Mg−Al−Pb and Mg−Al−Pb−Ce alloys in 3.5% NaCl solution at 298 K after removing corrosion products during hydrogen generation tests: (a) Mg−Al−Pb alloy; (b) Mg−Al−Pb−Ce alloy

3.4 Potential-time curves

Figure 6 shows the potential−time curves of Mg−Al−Pb and Mg−Al−Pb−Ce alloys at anodic current density of 180 mA/cm^2 in 3.5% NaCl solution. The current density of 180 mA/cm^2 was chosen to examine the discharge performance of magnesium alloy employed as anode for short-term high-power battery system [22]. According to Fig. 6, the discharge potentials of Mg−Al−Pb and Mg−Al−Pb−Ce alloys both shift toward negative direction in the beginning. The discharge potential of Mg−Al−Pb alloy shows obvious fluctuation at the first 100 s, indicating the complicated surface condition, such as oxide film. Meanwhile, the discharge potential of Mg−Al−Pb alloy expresses obvious

polarization, indicating the good stability of passive films formed by the corrosion products on the surface. After discharging for 400 s, the discharge potential of Mg−Al−Pb−Ce alloy gets into a steady state, which signifies the dynamic balance of formation and shedding for the discharge products [23]. The average discharge potentials of Mg−Al−Pb and Mg−Al−Pb−Ce alloys measured from potential−time curves are listed in Table 3. Undoubtedly, magnesium alloy with a negative discharge potential normally exhibits strong discharge activity [24]. According to Table 3, Mg−Al−Pb−Ce alloy expresses more negative potential than Mg−Al−Pb alloy. Thus, Ce addition increases the discharge activity of Mg−Al−Pb alloy.

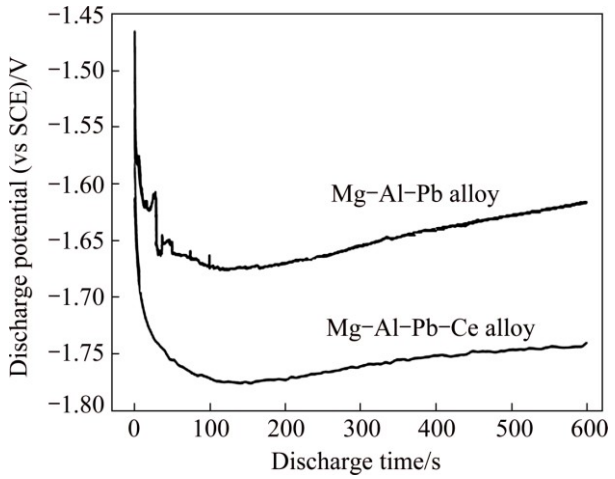

Fig. 6 Potential−time curves of Mg−Al−Pb and Mg−Al−Pb−Ce alloys in 3.5% NaCl solution at 298 K and anodic current density of 180 mA/cm^2

The microstructure of magnesium alloy generally plays a vital role in affecting its discharge behaviour. According to Fig. 1, Ce refines the grains, facilitates the formation of $Al_{11}Ce_3$ phase and inspires the homogeneous distribution of $Mg_{17}Al_{12}$ phase in Mg−Al−Pb alloy. ZHAO et al [25] suggested that the fine grain and uniform grain boundary were valuable to lead to high activated current of AZ31 magnesium alloy. Previous work also indicated that the fine grains of AP65 magnesium alloy produced by hot rolling or extrusion facilitated a negative shift of the discharge potential [5,18]. Moreover, the increasing amount of cathodic $Al_{11}Ce_3$ and $Mg_{17}Al_{12}$ second phases, greatly increases activity dissolution of magnesium matrix. Therefore, Mg−Al−Pb−Ce alloy provides more negative discharge potential and stronger discharge activity compared with Mg−Al−Pb alloy. The SE images displayed in Fig. 7 present the corrosion morphologies of Mg−Al−Pb and Mg−Al−Pb−Ce alloys discharged at 180 mA/cm^2 for 5 s after removing the discharge products. According to Figs. 7(a) and (b), it can be seen that round corrosion pits associated with active dissolution distribute on the surface of Mg−Al−Pb and Mg−Al−Pb−Ce alloys after tests. Some shallow corrosion pits with large size occur in Mg−Al−Pb alloy. They are discontinuous and their

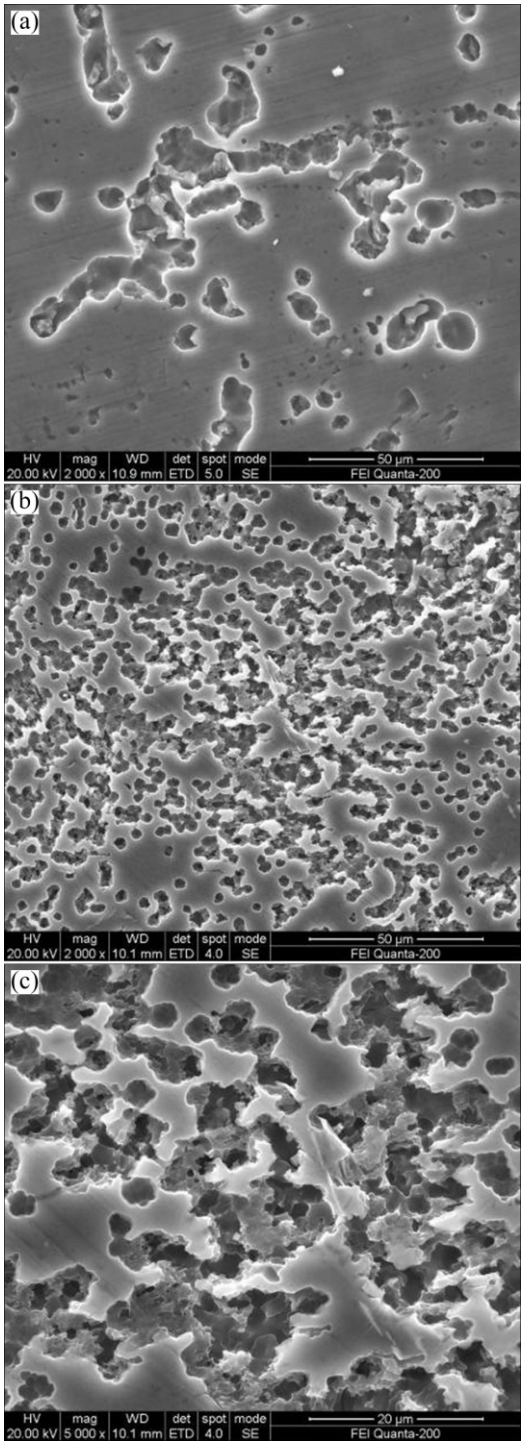

Fig. 7 Secondary electron (SE) images of Mg−Al−Pb and Mg−Al−Pb−Ce alloys in 3.5% NaCl solution at 298 K during galvanostatic discharge tests for 5 s after removing corrosion products: (a) Mg−Al−Pb alloy; (b) Mg−Al−Pb−Ce alloy; (c) Closed-up view of (b)

amount is far less than that in Mg−Al−Pb−Ce alloy. A lot of deep corrosion pits with small size occur in Mg−Al−Pb−Ce alloy. They are continuous and homogeneous in magnesium matrix. The difference between two kinds of corrosion pits morphologies indicates that general anode dissolution occurs in Mg−Al−Pb−Ce alloy, while Mg−Al−Pb alloy expresses localized attack in the beginning of discharge. The general corrosion morphology is normally related to a good discharge activity. Thus, Mg−Al−Pb−Ce alloy shows better discharge activity than Mg−Al−Pb alloy.

3.5 Utilization efficiency

The utilization efficiencies were tested in the course of galvanostatic discharge at an anodic current density of 180 mA/cm^2 for 1 h. The calculated utilization efficiencies of Mg−Al−Pb and Mg−Al−Pb−Ce alloys are summarized in Table 3. According to Table 3, the utilization efficiency of Mg−Al−Pb−Ce alloy at 180 mA/cm^2 reaches (74.7±0.4)%, which is higher than those of Mg−Al−Pb alloy (67.7±0.2)% and pure magnesium (62.2±0.5)%. Thus, Ce addition enhances the utilization efficiency of Mg−Al−Pb alloy in the course of discharge at a large current density.

During discharge process, hydrogen evolution corrosion and grain detachment severely decrease the utilization efficiency of magnesium alloys. Although in the immersion tests as described in Table 3, the hydrogen evolution rate of Mg−Al−Pb alloy is smaller than that of Mg−Al−Pb−Ce alloy. During discharge process at a certain current density, the hydrogen evolution reaction of magnesium alloys can be accelerated. Moreover, the detachment of metallic particles during discharge process severely decreases the utilization efficiency of magnesium alloys. The SE images displayed in Fig. 8 present the morphologies of Mg−Al−Pb and Mg−Al−Pb−Ce alloys discharged at 180 mA/cm^2 for 1 h after removing the discharge products. The surface morphology in Fig. 8(a) presents as polyporous honeycomb, indicating that Mg−Al−Pb alloy suffers severe corrosion with grain detachment from the alloy surface. The grain detachment increases the total mass loss and greatly decreases the utilization efficiency of Mg−Al−Pb alloy. According to Fig. 8(b), the corroded surface in Mg−Al−Pb−Ce alloy is smooth with some shallow corrosion holes, indicating that Mg−Al−Pb−Ce alloy dissolves uniformly during the discharge process. The existence of $Mg_{17}Al_{12}$ and $Al_{11}Ce_3$ phases in Mg−Al−Pb−Ce alloy certifies that these second phases do not detach from magnesium matrix easily in the discharge process. The result is consistent with the surface morphology of Mg−Al−Pb−Ce alloy after hydrogen evolution tests, as seen in Fig. 5(b). In that image, strip $Al_{11}Ce_3$ second phase is crisscross in magnesium matrix and remains during hydrogen evolution corrosion. Thus, Mg−Al−Pb−Ce alloy exhibits higher utilization efficiency in contrast with Mg−Al−Pb alloy.

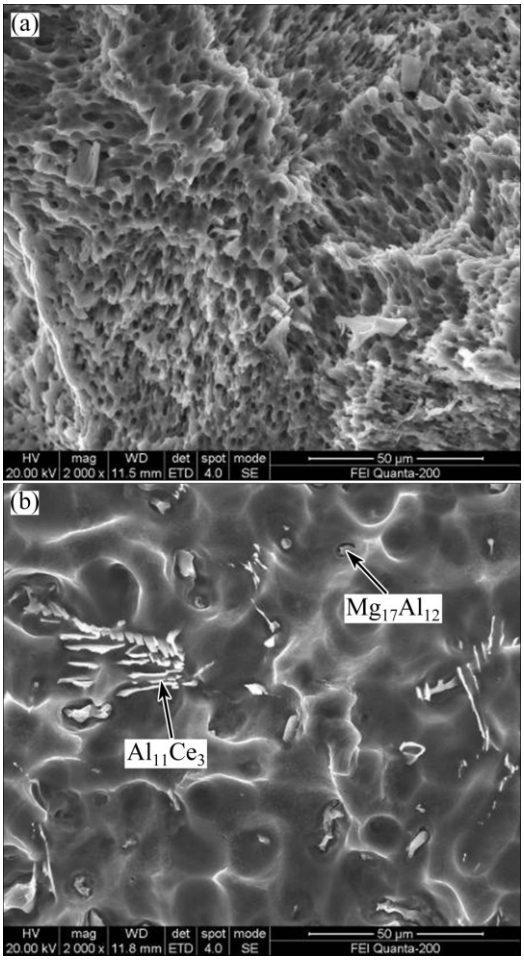

Fig. 8 SE images of surface morphologies of magnesium anodes discharged at current density of 180 mA/cm^2 for 1 h after removing discharge products: (a) Mg−Al−Pb alloy; (b) Mg−Al−Pb−Ce alloy

4 Conclusions

1) The addition of Ce to Mg−Al−Pb alloy refines the grain structure and promotes the formation of $Al_{11}Ce_3$ phase, which leads to the decreasing size and uniform distribution of $Mg_{17}Al_{12}$ phase.

2) The corrosion current density and hydrogen evolution rate of Mg−Al−Pb−Ce alloy are larger than Mg−Al−Pb alloy and the discharge activity of Mg−Al−Pb−Ce alloy at 180 mA/cm^2 is improved because of the refined grain and the increasing amount of cathodic second phases.

3) Larger utilization efficiency was found in Mg−Al−Pb−Ce alloy, while Mg−Al−Pb alloy has smaller

utilization efficiency due to the grain detachment during the discharge process. Hence, Mg−Al−Pb−Ce alloy is a promising candidate for the anode material of seawater battery.

References

[1] SHINOHARA M, ARAKIB E, MOCHIZUKIC M. Practical application of a sea-water battery in deep-sea basin and its performance [J]. Journal of Power Sources, 2009, 187: 253−260.

[2] QISREIN H, TORLEIF L, ERIK H. A long-range, autonomous underwater vehicle using magnesium fuel and oxygen from the sea [J]. Journal of Sources, 2004, 136: 232−239.

[3] GIRAUDET J, CLAVES D, GUERIN K, DUBOIS M, HOUDAYER A, MASIN F, HAMWI A. Magnesium batteries: Towards a first use of graphite fluorides [J]. Journal of Power Sources, 2007, 173: 592−598.

[4] FENG Yan, WANG Ri-chu, PENG Chao-qun, WANG Nai-guang, QIU Ke, ZHANG Jia-pei, ZHANG Chun. Researches and application of magnesium anode materials in seawater battery [J]. Transactions of Nonferrous Metals Society of China, 2012, 21(1): 259−268.

[5] WANG Nai-guang, WANG Ri-chu, PENG Chao-qun, FENG Yan, CHEN Bin. Effect of hot rolling and subsequent annealing on electrochemical discharge behavior of AP65 magnesium alloy as anode for seawater activated battery [J]. Corrosion Science, 2012, 64: 17−27.

[6] WANG Nai-guang, WANG Ri-chu, PENG Chao-qun, FENG Yan. Effect of manganese on discharge and corrosion performance of magnesium alloy AP65 as anode for seawater-activated battery [J]. Corrosion, 2012, 68: 388−397.

[7] WANG Nai-guang, WANG Ri-chu, PENG Chao-qun, FENG Yan. Corrosion behavior of magnesium alloy AP65 in 3.5% sodium chloride solution [J]. Journal of Materials Engineering and Performance, 2012, 21: 1300−1308.

[8] WU W X, JIN L, ZHANG Z Y, DING W J, DONG J. Grain growth and texture evolution during annealing in an indirect-extruded Mg−1Gd alloy [J]. Journal of Alloys and Compounds, 2014, 585: 111−119.

[9] ISSA A, SAAL J E, WOLVERTON C. Formation of high-strength β' precipitates in Mg-RE alloys: The role of the Mg/β'' interfacial instability [J]. Acta Materialia, 2015, 83: 75−86.

[10] NAM N D, KIM J G, SHIN K S, JUNG H C. The effect of rare earth additions on the electrochemical properties of Mg−5Al-based alloys [J]. Scripta Materialia, 2010, 63: 625−628.

[11] SUDHOLZ A D, GUSIEVA K, CHEN X B, MUDDLE B C, GIBSON M A, BIRBILIS N. Electrochemical bahaviour and corrosion of Mg−Y alloys [J]. Corrosion Science, 2011, 53: 2277−2282

[12] LV Yan-zhuo, XU Yan, CAO Dian-xue. The electrochemical behaviors of Mg, Mg−Li−Al−Ce and Mg−Li−Al−Ce−Y in sodium chloride solution [J]. Journal of Power Sources, 2011, 196(20): 8809−8814.

[13] LIU Wen-juan, CAO Fa-he, CHANG Lin-rong, ZHANG Zhao, ZHANG Jian-qing. Effect of rare earth element Ce and La on corrosion behavior of AM60 magnesium alloy [J]. Corrosion Science, 2009, 51: 1334−1343.

[14] LIU Wen-juan, CAO Fa-he, JIA Bing-li, ZHENG Li-yun, ZHANG Jian-qing, CAO Chu-nan, LI Xiao-gang. Corrosion behaviour of AM60 magnesium alloys containing Ce or La under thin electrolyte layers. Part 2: Corrosion product and characterization [J]. Corrosion Science, 2010, 52: 639−650.

[15] LIU Wen-juan, CAO Fa-he, CHEN An-an, CHANG Lin-rong, ZHANG Jian-qing, CAO Chu-nan, LI Xiao-gang. Corrosion behaviour of AM60 magnesium alloys containing Ce or La under thin electrolyte layers. Part 1: Microstructural characterization and electrochemical behavior [J]. Corrosion Science, 2010, 52: 627−638.

[16] MERT F, BLAWERT C, KAINER K U, HORT N. Influence of cerium additions on the corrosion behaviour of high pressure die cast AM50 alloy [J]. Corrosion Science, 2012, 65: 145−151.

[17] YAO Yu-fen, CHEN Chang-guo, LIU Yu-ping, SI Yu-jun. Effect of lanthanum salt on electrochemical behavior of AZ31 magnesium alloy [J]. Journal of Chinese Rare Earth Society, 2009, 27: 688−692.

[18] WANG Nai-guang, WANG Ri-chu, PENG Chao-qun, FENG Yan. Enhancement of the discharge performance of AP65 magnesium alloy anodes by hot extrusion [J]. Corrosion Science, 2014, 81: 85−95.

[19] WANG Nai-guang, WANG Ri-chu, PENG Chao-qun, FENG Yan, ZHANG Chun. Influence of aluminium and lead on activation of magnesium as anode [J]. Transactions of Nonferrous Metals Society of China, 2010, 20(8): 1403−1411.

[20] LIN M C, TSAI C Y, UAN J Y. Electrochemical behaviour and corrosion performance of Mg−Li−Al−Zn anodes with high Al composition [J]. Corrosion Science, 2009, 51: 2463−2472.

[21] KANNAN A S, MURALIDHARAN S, SARANGAPANI K, BALARAMACHANDRAN V, KAPALI V. Corrosion and anodic behaviour of zinc and its ternary alloys in alkaline battery electrolytes [J]. Journal of Power Sources, 1995, 57: 93−98.

[22] ZHAO Jun, YU Kun, HU Ya-nan, LI Shao-jun. Discharge behavior of Mg−4wt%Ga−2wt%Hg alloy as anode for seawater activated battery [J]. Electrochimica Acta, 2011, 56: 8224−8231.

[23] CAO Dian-xue, WU Lin, SUN Yong, WAGN Gui-ling, LÜ Yan-zhuo. Electrochemical behavior of Mg−Li, Mg−Li−Al and Mg−Li−Al−Ce in sodium chloride solution [J]. Journal of Power Sources, 2008, 177: 624−630.

[24] YU Kun, TAN Shi-yu, HU Ya-nan, CHEN Fu-wen, LI Shao-jun. Microstructure effects on the electrochemical corrosion properties of Mg−4.1%Ga−2.2%Hg alloy as the anode for seawater-activated batteries [J]. Corrosion Science, 2011, 53: 2035−2040.

[25] ZHAO Hong-yang, PEI Bian, JU Dong-ying. Electrochemical performance of magnesium alloy and its application on the sea water battery [J]. Journal of Environmental Science, 2009, 21(S): s88−s91.

Mg−Al−Pb 和 Mg−Al−Pb−Ce 阳极材料显微组织和腐蚀电化学性能

冯 艳[1,2]，刘 莉[1,2]，王日初[1,2]，彭超群[1,2]，王乃光[1,2]

1. 中南大学 材料科学与工程学院，长沙 410083；
2. 中南大学 有色金属材料科学与工程教育部重点实验室，长沙 410083

摘 要：Mg−Al−Pb 合金是一种应用于海水激活电池的镁阳极材料。为提高 Mg−Al−Pb 合金的电流效率，通过扫描电子显微镜和电化学测试方法研究 Ce 对 Mg−Al−Pb 合金显微组织和腐蚀电化学性能的影响。结果表明，Ce 元素促进了条状第二相 $Al_{11}Ce_3$ 的析出，使 $Mg_{17}Al_{12}$ 相在 Mg−Al−Pb−Ce 合金中分布更均匀，并细化了合金的显微组织。Ce 的添加提高了 Mg−Al−Pb 合金的放电活性，大量的第二相 $Al_{11}Ce_3$ 和 $Mg_{17}Al_{12}$ 使合金的微电偶腐蚀增强，从而导致 Mg−Al−Pb−Ce 合金具有较大的腐蚀电流密度和析氢速率。放电过程中 Mg−Al−Pb 合金存在晶粒脱落，相比之下，Mg−Al−Pb−Ce 合金具有更大的电流效率。

关键词：镁合金；海水电池；析氢速率；放电活性；电流效率

(Edited by Xiang-qun LI)